Inverse modeling of the 2021 spring super dust storms in East Asia

Jianbing Jin[1], Mijie Pang[1], Arjo Segers[2], Wei Han[3], Li Fang[1], Baojie Li[1], Haochuan Feng[4], Hai Xiang Lin[5], and Hong Liao[1]

[1]Jiangsu Key Laboratory of Atmospheric Environment Monitoring and Pollution Control, Jiangsu Collaborative Innovation Center of Atmospheric Environment and Equipment Technology, School of Environmental Science and Engineering, Nanjing University of Information Science and Technology, Nanjing, Jiangsu, China
[2]TNO, Department of Climate, Air and Sustainability, The Netherlands
[3]Numerical Weather Prediction Center, Chinese Meteorological Administration, Beijing, China
[4]Department of Sediment Research, China Institute of Water Resources and Hydropower Research, Beijing, China
[5]Delft Institute of Applied Mathematics, Delft University of Technology, Delft, the Netherlands

Correspondence: Hong Liao (hongliao@nuist.edu.cn)

Abstract. This spring, super dust storms reappeared in East Asia after being absent for a (two) decade(s). The event caused enormous losses both in Mongolia and in China. Accurate simulation of such super sandstorms is valuable for the quantification of health damages, aviation risks, and profound impacts on the Earth system, but also to reveal the driving climate and the process of desertification. However, accurate simulation of dust life cycles is challenging mainly due to imperfect knowledge of emissions. In this study, the emissions that lead to the 2021 spring dust storms are estimated through assimilation of MODIS AOD and ground-based PM_{10} concentration data. To be able to use the AOD observations to represent the dust load, an Ångström-based data screening is designed to select only observations that are dominated by dust. In addition, a non-dust AOD bias correction has been designed to remove the part of the AOD that could be attributed to other aerosols than dust. With this, the dust concentrations during the 2021 spring super storms could be reproduced and validated with concentration observations. The emission inversion results reveal that wind blown dust emissions originated from both China and Mongolia during spring 2021. Specifically, 18.3M and 27.2M ton of particles were released in Chinese desert and Mongolia desert respectively during these severe dust events. By source apportionment it has been estimated that 58% of the dust deposited in the densely populated Fenwei Plain (FWP) in the northern China originate from transnational transport from Mongolia desert. For the North China Plain (NCP), local Chinese desert play a less significant roles in the dust affection; the long-distance transport from Mongolia contributes for about 69% to the dust deposition in NCP, even if it locates more than 1000km away from the nearest Mongolian desert.

1 Introduction

Dust storms occurred as a result of wind erosion liberating dust particals from dry and barren surfaces (Shao et al., 1993). They are relatively common meteorological hazards in arid or semi-arid regions (World Meteorological Organization, 2019). Fine dust particles released from the ground could be lifted several kilometers high, and subsequently carried over long distances, sometimes even across continents (Zhang et al., 2018). The substantial amounts of dust particles, as well as irritating spores,

bacteria and viruses carried by the dust storms pose great threats to human health and agriculture (World Meteorological Organization, 2017). Next to these adverse health effects and property losses, the visibility reduction would cause severe disruption or disorders of the transportation and aviation systems (World Meteorological Organization, 2020). The dust cycle itself is also a key player in the Earth system by influencing the radiative balance (Wu et al., 2016) but also forest and ocean
5   ecosystems (Shao et al., 2011).

Driven by strong cyclones, dust storms form in the Mongolia and Gobi desert could affect East Asia following long distance transport patterns as can be seen in for example Fig.1(a). These events usually occur in spring time, when particles are more erodible under the circumstance of a dry season and sparse vegetation. The frequency and intensity of spring dust storms reached a peak from the 1950s to 1970s, and declined steadily later (Yin et al., 2021). In the past decade, the dust storms were
10   persistently rare, and only 2 strong events occurred in 2015 (Jin et al., 2018) and 2017 (Jin et al., 2019b). The declining trend in dust storm occurrence was co-driven by strict greenness controls in the northern China over the past decades (Shao et al., 2013), climate anomalies (Yin et al., 2021), synoptic disturbances, and other factors not yet explored. However, the ongoing land degradation and desertification in Mongolia (Han et al., 2021) is reported to aggravate the regional dust storms. In spring 2021 however, East Asia experienced an outbreak of severe dust storms after an absence of a (two) decade(s). Specifically,
15   three super events occurred during March 14 to 16, March 26 to 28 and April 14 to 15, which will be described in Section 2.1 later. The re-occurred spring super dust storms resulted in enormous losses directly. Taking the dust event in March 14-16 for example, 10 people were reported dead and hundred of people reported missing in Mongolia (Chen and Walsh, 2021); the PM_{10} pollutant level in Beijing was brought over 8000 $\mu g/m^3$, and 12 provinces in the northern China were affected with thousands of flights grounded and public transportation systems halted (Jin, 2021). To fully understand the reappeared dust storms is of
20   great interest to health professionals, aviation authorities and policy makers, which not only helps to evaluate property losses, adverse health effects and Earth system impacts, but also to reveal the climate-synoptic driving forces, and finally to build the next generation of the dust early warning system.

Numerical simulation models are commonly used to study dust life cycles. Such models usually consists of an atmospheric transport model that is able to simulate aerosol concentrations, coupled to a dust emission module. The underlying model is
25   often a chemistry-transport model (CTM) which is already used to calculate concentrations of air pollutants, with dust just one of the aerosol species included. Substantial effort has been paid to develop dust models, especially to the dust emission parameterzation which is the most uncertain element in simulating the dust concentrations. Since the early 1990s, several dust emission schemes have been introduced, e.g., MB95 (Marticorena and Bergametti, 1995), Shao96/Shao04 (Shao et al., 1996; Shao, 2004), Ginoux01 (Ginoux et al., 2001) and Zender03 (Zender, 2003). Such emission parameterizations have been
30   included in many global or regional atmospheric transport models, e.g., ECMWF's Integrated Forecast System (IFS) (Morcrette et al., 2008b, a, 2009), BSCDREAM8b (Pérez et al., 2006; Mona et al., 2014), CUACE/Dust(Zhou et al., 2008; Gong and Zhang, 2008), GEOS-Chem (Fairlie et al., 2007), and LOTOS-EUROS (Timmermans et al., 2017; Manders et al., 2017) as will be used in this study. Due to insufficient knowledge of the actual dust emission and transport, and due to limitations to computing resources to resolve finest-scale variabilities, huge differencec might occure when simulations are compared to
35   observations (Niu et al., 2008; Huneeus et al., 2011).

Recent advances in sensor technologies and the continuously decreasing cost of electronic devices have made large scale measurements of dust feasible. For dust storms over East Asia, important observation includes ground-based aerosol optical properties from the AErosol RObotic NETwork (AERONET) (Dubovik et al., 2000) and Sun-sky radiometer Observation NETwork (SONET) (Li et al., 2018), PM_{10} concentration from the China Ministry of Environmental Protection (MEP) air quality

5 monitoring network (Jin et al., 2018), satellite remote sensing data from polar-orbiting instruments (e.g., Moderate Resolution Imaging Spectroradiometer (MODIS) (Remer et al., 2005) and Cloud-Aerosol Lidar and Infrared Pathfinder Satellite Observations (CALIPSO) (Winker et al., 2007)), and from geostationary platforms (e.g., Himawari-8 (Bessho et al., 2016) and FY-4 AOPs (Min et al., 2017)). These various types of observations have been used next the simulation models to analyze the dust storms (Ginoux et al., 2012; Gkikas et al., 2021). Despite their significant roles in characterizing the atmospheric dust load, us-

10 ing only the measurements is not sufficient to obtain a complete four-dimensional insight in the dust plumes, because either the measurements do not cover all area (surface network), only observe once or twice a day (polar orbiting satellites), or observe only vertically integrated quantities (AOD).

Instead of studying dust storms with either simulation models or observations only, it is useful to combine the measurements and the simulations through data assimilation (Kalnay, 2002). For the purpose of dust storm simulations, the measurements

15 could be used to decrease the uncertainty in the emissions such that the optimized simulation is in better agreement with those measurements (Gong and Zhang, 2008; Lin et al., 2008). For instance, aerosol products from the MODIS instrument onboard the polar orbiting satellite Terra and Aqua have been widely applied in global or East Asia dust storm assimilation (Di Tomaso et al., 2017; Yumimoto and Takemura, 2015). The geostationary Himawari-8 data has recently also gained popularity and has been used in dust storm detection and assimilation (Yumimoto et al., 2016). In our previous studies described in Jin et al. (2018,

20 2019a), the ground-based PM_{10} concentration data was assimilated, to estimate the dust source emission for a sandstorm in 2015 over East Asia. Himawari-8 AODs were also assimilated to nudge the dust emission, and the necessity of removing those AODs in cloudy environment is emphasised in Jin et al. (2019b). An adjoint model was applied to construct a background covariance that was better able to describe the potential source regions for dust emission (Jin et al., 2020). Meanwhile, an imaging morphing based assimilation method was designed which effectively corrected the position error caused in the long-

25 distance dust plume transport (Jin et al., 2021).

While various kinds of dust or aerosol measurements where used in these assimilation experiments, most of these assimilated only one type of observation at a time. For the sandstorms in East Asia, however, any of the aforementioned measurements cannot provides sufficient information to track these short-term and fast-changing dust plumes completely. For a case in point, the China MEP air quality monitoring network has over 1700 sites for PM_{10} concentrations by now, but these are mainly

30 located in the downwind and densely populated regions, which are far away from the source region of dust in East Asia (the Mongolia and Gobi deserts that can be seen in Fig. 1)(a). The network therefore only measure the dust plume when it is already transported to the downwind urban regions; hence, it is of limited help to characterize the plume near the source regions in rural areas. Besides, the ground-based PM_{10} data only represents the surface dust concentrations and lacks information on the vertical structure. AERONET and SONET instruments provide some information on the vertical structure via column integrated

35 observations, but the network is much sparser than the PM_{10} network, and most of the sites are also far away from the source

regions too. The MODIS satellite products provide a global coverage, but again only information on the total column and therefore no estimate of the plume height or thickness. These polar orbiting instruments also have a limited temporal coverage; for example, the MODIS Aqua and Terra platforms pass by only around 10:30 and 13:30 (local time). Designed with the wide observing coverage and high temporal resolution, geostationary measuring instruments provide valuable information.

5 However, large uncertainties were found in the Himawari-8 product due to uncertainty in assumptions on aerosol models and surface reflectance estimation in the retrieval algorithm (Zhang et al., 2019). This was also found in Jin et al. (2019b): a strict observation selection was necessary when assimilating the Himawari-8 AOD values.

Another challenge for dust assimilation is the proper definition of the observations. In general, the commonly used data assimilation schemes all rely on the basic assumption of an unbiased observation. However, all the aforementioned observations,

10 e.g., AOD and PM_{10} concentration, do not only measure dust aerosols, but rather actually the sum of the dust and other fine particles. These originate from for example anthropogenic activities, e.g., industry, vehicles, and households, and from natural sources such as wildfires and sea spray. These particles are referred to the non-dust fraction in the total aerosols in our study. In the presence of a non-dust biase, it is impossible to attribute the difference between the *a priori* simulation and an observation to either this bias or to model deficiencies. The non-dust bias might lead to assimilations that diverge from reality (Lorente-

15 Plazas and Hacker, 2017). However, aerosol measurements are usually directly assimilated, and little progress has been made in bias correction of fully aerosol measurements for their use in dust storm assimilation. Lin et al. (2008) selected only PM_{10} observations for assimilation when at least one occurrence of dust clouds was reported by the local stations. Both machine learning tools and chemical transport models were used for modeling the dynamic non-dust aerosol levels in the PM_{10} concentration measurements, the bias-corrected observations subsequently resulted in more promising assimilation analysis in Jin

20 et al. (2019a). Some efforts have been made to exclude those 'polluted' AODs induced by cloud scenes in the dust assimilation (Jin et al., 2019b); nevertheless, the issue of a non-dust AOD bias remains to large extent unresolved.

To analyze the outbreak of super dust storms in 2021 spring, an emission inversion will be performed through assimilation of multiple observation types. Both the MODIS AOD and the ground-based PM_{10} concentration observations will be used, each providing a different view on the dust plumes. The added value of assimilating them together is obvious: PM_{10} data gives

25 a high temporal resolution while MODIS AOD provides dust load information with a wide spatial coverage. To use the AODs for representing the dust load, an data quality control is designed, which consists of an Ångström-based data screening and a non-dust AOD bias correction. The former is capable of selecting those coarse-mode dust AOD values, and excludes the pixels dominated by fine-mode aerosol from non-dust sources, while the latter focuses on removing the non-dust baseline in the selected AOD. Similar for PM_{10} a non-dust bias correction as used in Jin et al. (2019a, 2021) is adopted in this work.

30 Based on the posterior emission field obtained in the inversion, the spatial pattern of the emission analyzed for the three events studied, and the active source regions are identified. In addition, source apportionment simulations are performed, in which the contribution of dust emissions from either Mongolia or China to the dust deposition is calculated for two mega-city clusters, the North China Plain (NCP) and the Fenwei Plain (FWP).

The paper is organized as follows. Section 2 introduces the three super dust events that occurred in this spring, as well

35 as the available dust observations from MODIS and ground-based PM_{10} networks measuring the dust loading from different

Table 1. Descriptions of the three severe dust storm events that occurred in China in spring 2021. Timezone is China Stand Time (CST))

dust event	Timeline	Affected regions	Highest PM$_{10}$ [μg/m^3]	assimilation window
SD1	2021 March 15	NCP	9993	March 13, 00:00 to March 15, 23:00
SD2	2021 March 28	NCP, FWP	9985	March 26, 00:00 to March 28, 23:00
SD3	2021 April 15	NCP, FWP	4113	April 14, 00:00 to April 15, 23:00

perspectives. Before AOD is assimilated, quality control combining an Ångström-based screen and a non-dust bias correction are designed to ensure that the observations are representative for the dust load. A brief description of our dust simulation model (LOTOS-EUROS/dust) is presented as well. Section 3 reviews the 4DVar data assimilation based emission inversion system. In Section 4, the posterior emission field and the estimated AOD and surface dust concentration simulation are evaluated and

5   discussed. A source apportionment study is performed to obtain information about dust pollution sources and the amount in which they contribute to ambient air pollution in the northern China. Focusing on NCP and FWP, their dominant dust source are identified here.

2   Dust events, measurements, and model

2.1   Dust events of Spring 2021

10   The Fenwei Plain (FWP) and the North Chinese Plain (NCP) experienced the most dust affection in China since they face the dust source regions as shown in Fig. 1(a). Fig.1(b) shows the recorded PM$_{10}$ concentration average during spring (March-May) in NCP and FWP over 2019-2021. In spite of ongoing air pollutant reduction measures, the PM$_{10}$ levels in NCP and FWP both reached their highest average values of 123 and 119 μg/m^3 in 2021. These mean values are 34% and 27% higher than the means of the previous two years. The reason for this is that East Asia suffered an outbreak of dust storms in the 2021 Spring season,

15   including three large-scale and severe ones. The timeline in Table.1 shows that these three dust events occurred around March 15, March 28 and April 15, and each of them lasted 2 to 3 day. The highest PM$_{10}$ concentrations reported by the ground-based air quality monitoring network shown in Fig.1 reached values of 9993, 9985, and 4113 μg/m^3. In this study, the three events are referred to as SD1, SD2 and SD3, respectively.

    The three dust storms will be studied by combining model simulations and AOD/PM$_{10}$ observations using assimilation, in

20   order to identify the emission sources that affects the densely populated regions in northern China.

2.2   Ground-based PM$_{10}$ observations

A huge number of ground-based stations measuring air quality indicators have been established by the China Ministry of Environmental Protection (MEP) since 2013. At present, the monitoring network has grown up to 1800 monitoring sites covering China, of which a part is shown in Fig.1(a). The PM$_{10}$ concentrations observed by the network hence provide valuable

a

b
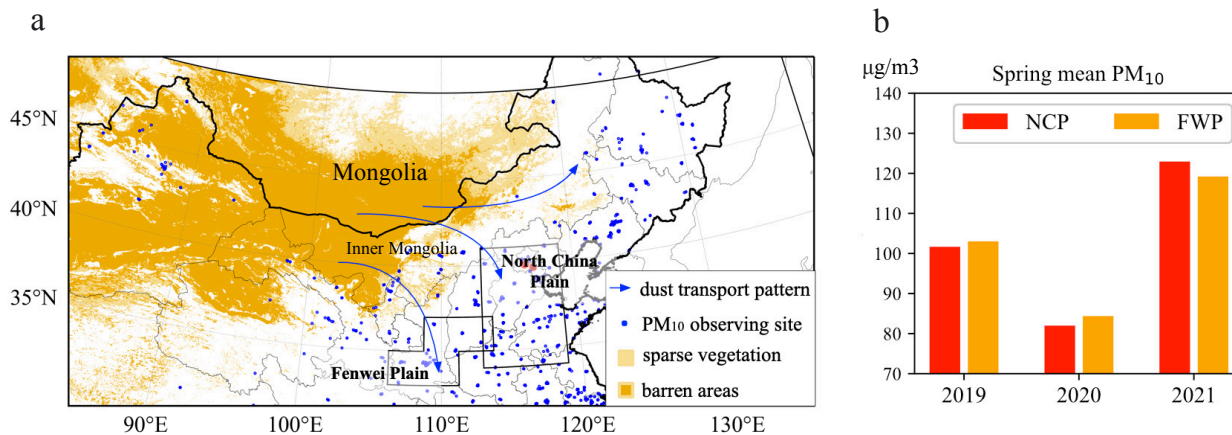
Figure 1. (a) Distribution of the potential dust emission source (barren and sparse vegetation landcover) over East Asia and the China MEP observing network over northern China; (b) The spring (March-May) mean PM_{10} concentration observations over NCP and FWP from 2019 to 2021.

information on the dust storms. Snapshots of the PM_{10} measurements for SD1, SD2 and SD3 can be found in Fig.2(a.1), Fig.3(a.1) and Fig.4(a.1), respectively. In the observations it is clearly visible where the dust plume is located and how it moves through the regions.

It should be kept in mind that these PM_{10} measurements are actually a sum of dust and other airborne particles like black
5 carbon, sulfate, etc. The PM_{10} data therefore cannot be used directly to represent the dust load. In a previous study (Jin et al., 2019a) it has been shown that removing the non-dust baseline from PM_{10} observations will lead to a more accurate assimilation result, especially in case that dust aerosol is not dominant. In this study, the same observational bias correction is performed to make the PM_{10} measurements fully representative of the dust loads.

The PM_{10} bias correction takes two steps. First, non-dust aerosol levels are calculated using a model simulation with a
10 configuration for air quality simulation (as will be described in Section 2.4), but with the dust tracers disabled. Second, using these simulations, bias-corrected dust observations were calculated by subtracting the non-dust loads from the original PM_{10} observations.

The non-dust aerosol surface concentrations from the simulations, and the dust-only bias-corrected observations of PM_{10} are available in Supplementary Fig.S1(a), Fig.S2(a) and Fig.S3(a). As example, as shown in Fig.S1(a), during the SD1 event
15 the non-dust aerosols were also carried southward and ahead of the dust plume due to the strong winds. The bias-corrected PM_{10} data clearly shows the shape of the dust plume. The shape of the simulated *a priori* dust plume at March 15 10:00 shown in Fig.2(a.2) matches well with the observed shape, although the dust concentrations are sometimes very different; this will be discussed in more detail in Section 2.4. Similar features are seen in Fig.S2(a) and Fig.S3(a) for the other events as well.

2.3 MODIS AOD observations

2.3.1 MODIS Deep Blue AOD product

The Moderate Resolution Imaging Spectroradiometer (MODIS) satellite instruments (Justice et al., 1998) on board of the polar orbiting satellites Terra and Aqua measure atmosphere reflectance at several wavelengths in the range from visible to the near-infrared. The aerosol properties that are retrieved from the MODIS observations have provided high-quality data since 2000 (Terra) and 2002 (Aqua). Designed with a wide swath (≈2330km), MODIS provides near-global observations almost on a daily basis. In this study, the Deep Blue dataset, in the newest MODIS Collection 6.1 operational Level-2 aerosol product is used. The Deep Blue dataset is generated by the Enhanced Deep Blue algorithm (Hsu et al., 2013; Sayer et al., 2014), reporting retrievals over all cloud-free and snow-free land surfaces at a resolution of 10 km. The MODIS Deep Blue dataset is widely used in dust source identification (Ginoux et al., 2012), dust model calibration (Zhang et al., 2018), and emission inversion (Yumimoto and Takemura, 2015; Di Tomaso et al., 2017) and dust field reanalysis (Di Tomaso et al., 2021) through data assimilation.

Snapshots of the MODIS Deep Blue AOD for the SD1, SD2 and SD3 could be found in Fig.2(b.1-c.1), Fig.3(b.1) and 4(b.1). For each of the three events, MODIS AOD provides valuable information for a large part of the domain of interest. For instance, the SD2 plume position and intensity at March 28, 11:00 are clearly identified in Fig. 3(b.1), while the SD3 plume at April 15, 11:00 is observed clearly in Fig. 4(b.1). The two AOD scans in Fig.2(b.1-c.1) together also provides the general spatial pattern of the dust plume.

Compared to the ground-based PM_{10} measurements, satellite instruments are designed with a larger observing coverage. However, they also have higher uncertainties in representing the aerosol/dust load (Jin et al., 2019b). In most of the dust model evaluation/calibration using the satellite data, AOD measurements are directly used for comparing to simulated dust AODs and analyzing the dust strengths. For those regions affected by the severe dust storm, it would be reliable to approximate the dust AODs using the AOD measurements since the amounts of non-dust aerosols are negligible compared to the dust loading; for those areas where dust is not the dominant aerosol, it is then necessary to perform the dust/non-dust AOD discrimination.

2.3.2 AOD quality control

While aerosol originating from biomass-burning, urban pollution, and biogenic sources consist mainly of fine-mode particles (with a radius less than 1 μm), the aerosols in a dust plume are mainly in the coarse modes (particle radius larger than 1 μm) (Dubovik et al., 2002; Jin et al., 2019a). The dominance of one mode over the other can be measured with the Ångström wavelength exponent α (Schuster et al., 2006; Saide et al., 2013; Liu et al., 2019), which describes how the optical thickness depends on the wavelength of the incident light. Ångström is at a range from -0.5 to 2.5, and inversely related to the average size of the measured aerosol: the smaller the particles, the larger the exponent. Eck et al. (1999) used α=0.5 as the threshold for an aerosol mixture dominated by dust, while Schepanski et al. (2007) used α=0.6 to detect the presence of dust particles. Ginoux et al. (2012) used α=0 to select areas dominated by dust in a single-modal distribution of coarse particles.

Fig.5 shows the four snapshots of retrieved Ångström exponents corresponding to the of AOD values of Fig.2(b.1-c.1), Fig.3(b.1) and Fig.4(b.1). In general, the locations of low-Ångström values correspond with the high AOD values the dust plumes. For example for the snapshot in Fig.5(d), it indicates that a plume of coarse aerosols stays in the Inner Mongolia provinces of China, while fine aerosols are more dominant in the southern regions. This matches with the dust simulation that

5   are shown in Fig. 4(b.2). This gives confidence in using the Ångström values for the discrimination between dust and non-dust AOD.

To be able to use the AOD observations in an assimilation focusing on dust only, an Ångström-based data screening and a non-dust AOD bias correction has been developed and applied. The screening and bias-correction procedures are performed after each other. First the Ångström-based screening selects the pixels with $\alpha < 0.5$ assuming that these are the ones that

10   are dominated by (coarse mode) dust. For these pixels a bias-corrected AOD is calculated by subtracting a non-dust AOD fraction from the selected AODs. Similar to the non-dust PM_{10} simulation, these non-dust AOD baselines are also calculated using a full-chemistry LOTOS-EUROS simulation with the dust tracers disabled. Finally, to make the AOD data resolution consistent with the model, the MODIS Deep Blue AODs are coarsened by taking the average over the 0.25×0.25 model grid cell. Snapshots of the non-dust AOD simulation and the bias-corrected AOD measurements for assimilation can be found in

15   Supplementary Figures S1(b-c), S2(b), and S3(b).

2.4 Dust simulation model

The regional chemical transport model LOTOS-EUROS v2.1 (Manders et al., 2017) is used to simulate dust concentrations. LOTOS-EUROS has been used for a wide range of applications supporting scientific research and operational air quality forecasts over Europe, China, and other regions. Daily operational forecasts over China used to be released via the Mar-

20   coPolo–Panda projects (Timmermans et al., 2017; Brasseur et al., 2019). Additionally, it is also implemented in the World Meteorological Organization (WMO) Sand and Dust Storm Warning Advisory and Assessment System to provide short-time forecasting of the dust load over the area of North Africa, Middle East, and Europe; the online forecast product is delivered via http://sds-was.aemet.es/forecast-products/dust-forecasts (last access: July 2021).

To simulate dust concentrations over East Asia, the model is configured on a domain from 15°N to 50°N and 70 °E to 140

25   °E, with a resolution of 0.25°×0.25°. Vertically, the model consists of eight layers, with a top at 10 km. Our regional model has zero boundary conditions by assuming all dust aerosols are emitted regionally and the external dust flows can be ignored. Though BSC-DREAM8b simulation, which is released via https://ess.bsc.es/bsc-dust-daily-forecast (last access: Jan 2022), indicates that part of the dust plume released in Middle East is likely to be transported to the western China during SD1, but not far away to FWP or NCP. Boundary conditions from a global dust model are in demand if we are focusing on the western

30   China in our future work. The dust simulation is driven by European Centre for Medium-Ranged Weather Forecasts (ECMWF) operational forecasts over 3–12 h, retrieved at a regular longitude–latitude grid with a resolution of about 7 km. An interface to the ECMWF output set is designed, which not only interpolates the default 3h ECMWF short-term forecast meteorology to hourly values but also averages the forecast to fit the LOTOS-EUROS spatial resolutions (Manders et al., 2017). Physical processes included are wind-blown dust emission, diffusion, advection, dry and wet deposition, and sedimentation.
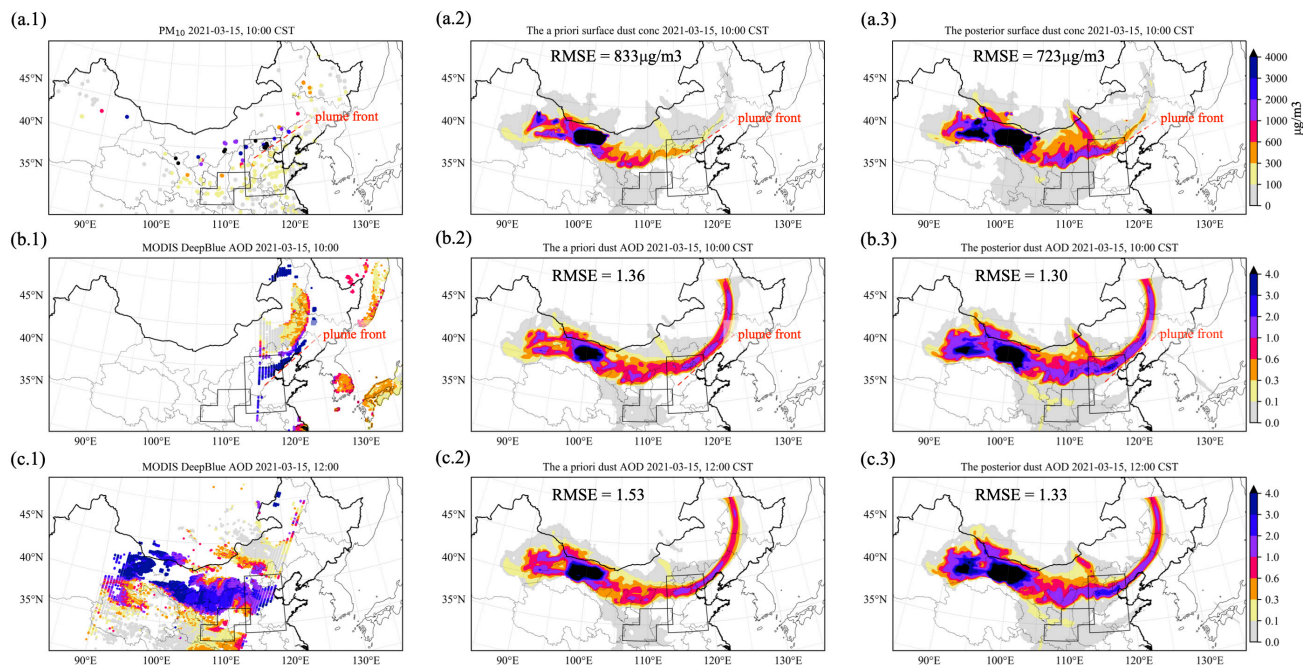
Figure 2. Snapshots of observations and simulations during severe dust event 1 (SD1) at 2021 March 15. Row (a) shows PM$_{10}$ concentrations observed by ground network at 10:00 CST (column 1), and *a priori* (column 2) and *posterior* (column 3) simulations by LOTOS-EUROS/dust model. Similar, row (b) shows for the same hour AOD at 550nm from MODIS Deep Blue observations (column 1), and simulations (columns 2-3) at 10:00; row (c) shows the same for the MODIS overpass at 12:00.
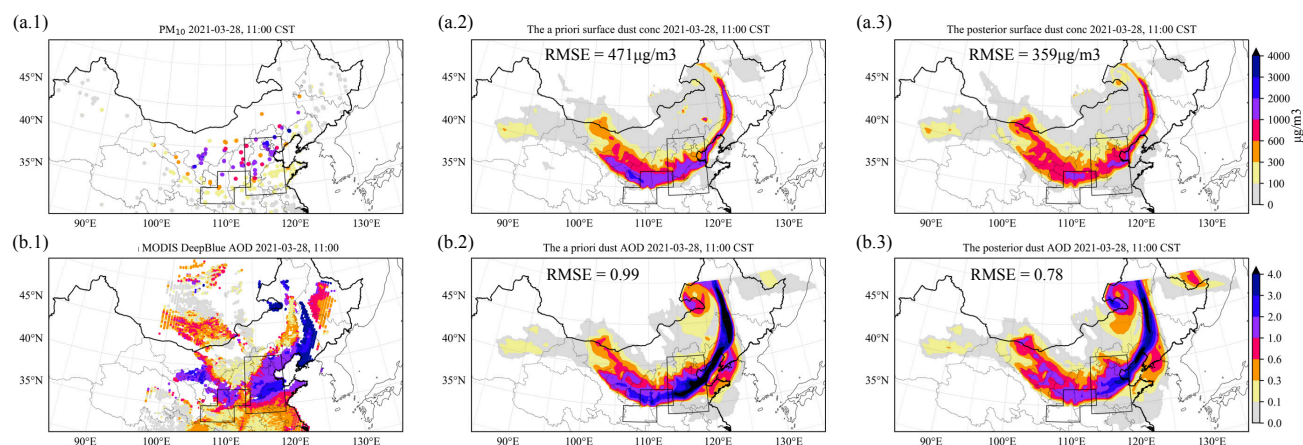
Figure 3. Snapshots of observations and simulations during severe dust event 2 (SD2) at 2021 March 28. Row (a) shows PM$_{10}$ concentrations observed by ground network at 11:00 CST (column 1), *a priori* (column 2) and *posterior* (column 3) simulations by LOTOS-EUROS/dust model. Row (b) shows for the same hour AOD at 550nm from MODIS Deep Blue observations (column 1), and simulations (columns 2-3).
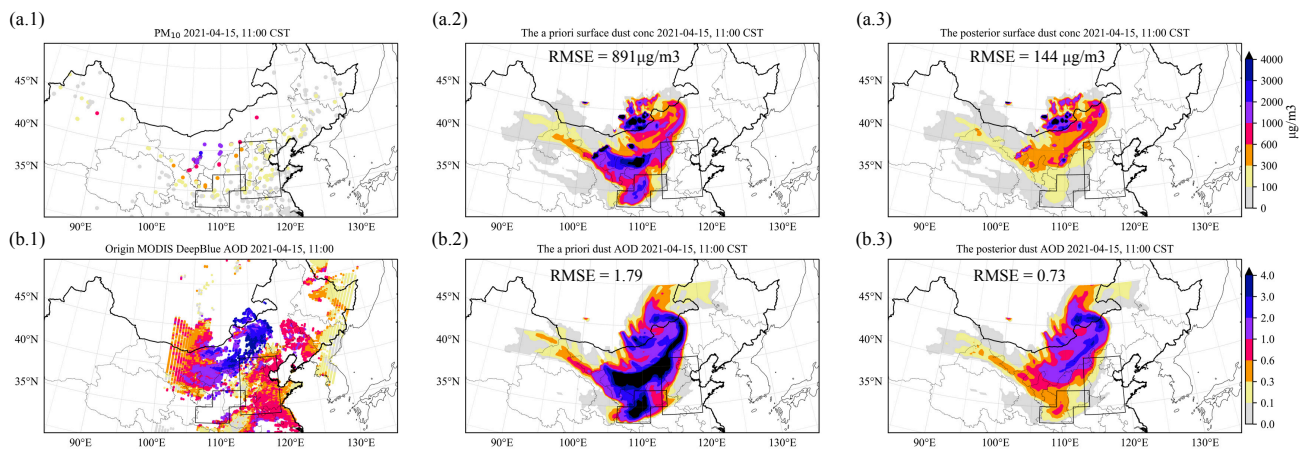
Figure 4. Snapshots of observations and simulations during severe dust event 3 (SD3) at 2021 April 15. Row (a) shows PM$_{10}$ concentrations observed by ground network at 11:00 CST (column 1), *a priori* (column 2) and *posterior* (column 3) simulations by LOTOS-EUROS/dust model. Row (b) shows for the same hour AOD at 550nm from MODIS Deep Blue observations (column 1), and simulations (columns 2-3).
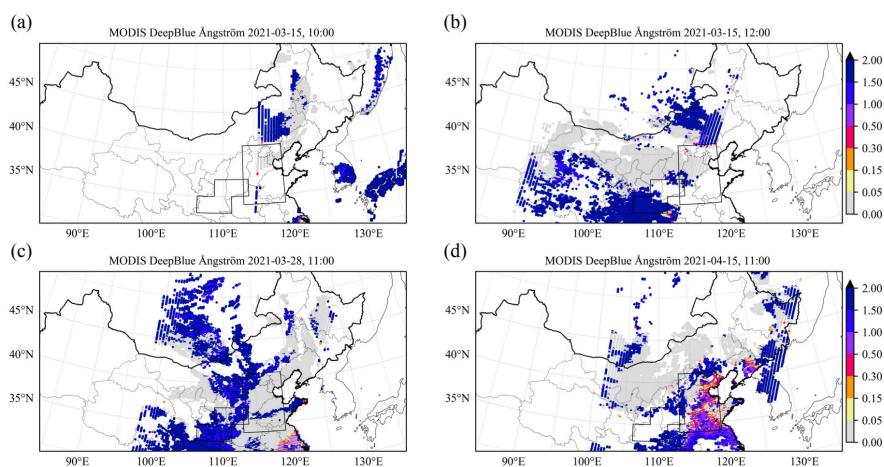
Figure 5. Snapshots of MODIS Deep Blue Ångström exponent accompanying AOD scenes shown in Fig.2(a.1-b.1), Fig.3(a.1) and Fig.4(a.1).

2.5 Dust emission and uncertainty

The goal of this work is to calculate the optimal emission field that best fits the *a priori* model simulation and the observation. It is then necessary to define and quantify the uncertainty in the dust simulations. In this study, we define the main model uncertainty to be in the parametrization of the dust emissions. Although other model processes such as transport and deposition are uncertain too, for the events studied here these assumed to be of less importance than the location and the intensity of dust emission.

The physical basis of the dust emission model adopted in LOTOS-EUROS is the parameterization scheme by (Zender, 2003). The dust flux f is calculated as a function of horizontal saltation f_h (Marticorena and Bergametti, 1995), the sandblasting efficiency a, a terrain preference $\mathcal{S}$, and an erodible surface fraction $\mathcal{C}$:

$$f = f_h \cdot a \cdot \mathcal{S} \cdot \mathcal{C} \tag{1}$$

The dust saltation rate $\mathcal{F}_h$ is proportional to the third power of the wind friction velocity u, as long as this exceeds a certain (surface depended) friction velocity threshold u_t:

$$f_h = \begin{cases} 0 & u \leq u_t \\ \frac{p_a}{g} \, u^3 \left(1 + \frac{u_t}{u}\right) \left(1 - \frac{u_t^2}{u^2}\right) & u > u_t \end{cases} \tag{2}$$

The friction velocity threshold controls if dust is released from a surface at all, and if it is, how strong the emission is. In Jin et al. (2018) it was shown that the uncertainty in the friction velocity threshold parametrization is the main reason that prohibits accurate dust emission forecasts. Although other controlling factors, e.g., the wind field uncertainty, will also introduce uncertainty in the emission partially, these were found to be of less important in the emission error quantification (Jin et al., 2019b).

3 Data assimilation algorithms

3.1 Assimilation method

The assimilation system that will be used to combine PM_{10} and AOD measurements with dust simulations, is based on the reduced-tangent-linearization four-dimensional variational (4DVar) data assimilation developed in (Jin et al., 2018). The goal of the 4DVar technique is to find the maximum likelihood estimation of a state vector, which is here the dust emission field $\boldsymbol{f}$, given both the available AOD and PM_{10} measurements over a time window. The optimal emission $\boldsymbol{f}$ is calculated by minimizing the cost function:

$$\mathcal{J}(\boldsymbol{f}) = \mathcal{J}_b(\boldsymbol{f}) + \mathcal{J}_o^{\text{PM}}(\boldsymbol{f}) + \mathcal{J}_o^{\text{AOD}}(\boldsymbol{f}) \tag{3}$$

In here, $\mathcal{J}_b$ represents the background term while $\mathcal{J}_o^{\mathrm{PM}}$ and $\mathcal{J}_o^{\mathrm{AOD}}$ quantify mismatch between dust simulation and PM$_{10}$/AOD measurements as follows:

$$\mathcal{J}_b(\boldsymbol{f}) = \frac{1}{2}(\boldsymbol{f} - \boldsymbol{f}_b)^{\mathrm{T}}\mathbf{B}^{-1}(\boldsymbol{f} - \boldsymbol{f}_b) \tag{4}$$

$$\mathcal{J}_o^{\mathrm{PM}}(\boldsymbol{f}) = \frac{1}{2}\sum_{i=1}^{m}\{\boldsymbol{y}_i^{\mathrm{PM}} - \mathcal{H}_i^{\mathrm{PM}}\mathcal{M}_i(\boldsymbol{f})\}^{\mathrm{T}}\,\mathbf{O}^{\mathrm{PM}^{-1}}_i\{\boldsymbol{y}_i^{\mathrm{PM}} - \mathcal{H}_i^{\mathrm{PM}}\mathcal{M}_i(\boldsymbol{f})\} \tag{5}$$

$$\mathcal{J}_o^{\mathrm{AOD}}(\boldsymbol{f}) = \frac{1}{2}\sum_{i=1}^{n}\{\boldsymbol{y}_i^{\mathrm{AOD}} - \mathcal{H}_i^{\mathrm{AOD}}\mathcal{M}_i(\boldsymbol{f})\}^{\mathrm{T}}\,\mathbf{O}^{\mathrm{AOD}^{-1}}_i\{\boldsymbol{y}_i^{\mathrm{AOD}} - \mathcal{H}_i^{\mathrm{AOD}}\mathcal{M}_i(\boldsymbol{f})\} \tag{6}$$

In $\mathcal{J}_b$, $\boldsymbol{f}_b$ represents the *a priori* or *background* dust emission vector which follows the calculation described in Section 2.4. As in Jin et al. (2018), the errors in dust emission field are assumed to be only caused by the uncertainty in the friction velocity threshold u_t in Eq.2, and the same assumptions on the uncertainty are used to build an emission error covariance using an ensemble of perturbation simulations. In each ensemble member, the threshold u_t is perturbed with a spatially varying multiplicative factor β which is configured with a mean 1 and a standard deviation 0.1, and with a distance-based spatial correlation with a length scale of 300 km.

In the observation terms $\mathcal{J}_o^{\mathrm{PM}}$ and $\mathcal{J}_o^{\mathrm{AOD}}$ of the cost function, m and n are the number of time steps within the assimilation window; $\boldsymbol{y}^{\mathrm{PM}}$ and $\boldsymbol{y}^{\mathrm{AOD}}$ contain the pre-processed PM$_{10}$ and MODIS AOD measurements; $\mathcal{M}$ denotes the LOTOS-EUROS/dust transport model that is driven by the emission $\boldsymbol{f}$, and $\mathcal{H}^{\mathrm{PM}}$ and $\mathcal{H}^{\mathrm{AOD}}$ are the observation operators that convert simulated model concentrations into PM$_{10}$ and AOD observation space. The PM$_{10}$ and AOD observation mismatch term are weighted by observation error covariance $\mathbf{O}^{\mathrm{PM}}$ and $\mathbf{O}^{\mathrm{AOD}}$. The uncertainties in the observations are assumed to be independent, and hence both $\mathbf{O}^{\mathrm{PM}}$ and $\mathbf{O}^{\mathrm{AOD}}$ are diagonal matrices. The individual elements in $\mathbf{O}^{\mathrm{PM}}$ follows the PM$_{10}$ uncertainty choice proposed in (Jin et al., 2018), while the uncertainty of AOD measurements are taken directly from the MODIS Deep Blue product. Details concerning the dust emission calculation, uncertainty source identification and cost function minimization in our 4DVar data assimilation algorithm could be found in Jin et al. (2018, 2019b).

After the optimal emissions have been obtained that minimize the cost function, a *posterior* simulation with the LOTOS-EUROS/dust model is performed using the optimized emissions.

3.2 Assimilation window

Table 1 shows the timeline of the three severe dust events studied here. These dust events have a short duration, and therefore a single assimilation window with a length of 72, 72 and 48 hours are used, respectively. Dust emissions occur at the start of the assimilation window when a plume is lifted high to be carried downwind. The PM$_{10}$ network is only able to observe the plume when it has moved downwind, and is already far away from the source region. Therefore, assimilation windows covering both the time of dust emission and the moment of observation are necessary.

4 Results and discussions

4.1 Dust storm inverse modeling

Using the assimilation system introduced in Section 2.2 and Section 3, the emission inversions have been performed by assimilation the bias-corrected PM_{10} and MODIS AODs processed in Section 2.3. First, the posterior emission analysis is carried

5 out in Section 4.1.1, then the dust simulation driven by the posterior emission result are illustrated in Section 4.1.2.

4.1.1 Dust emission analysis

To assess the spatial pattern of the dust emission, the accumulated emissions over the assimilation window are calculated for each of the dust events. Fig.6 shows the map of the a priori and posterior accumulated dust emission in SD1 to SD3 over the potential source regions. The a priori model simulation indicates dust emission mainly took place over both the Alxa

10 desert in China and the Mongolia desert for SD1, with a maximum in 221 g/m^2 in China and 286 g/m^2 in Mongolia. Through assimilating the MODIS AODs and ground-based PM_{10} concentration measurements, a new the emission field is estimated, with more grid cells from which emission took place located in the Alxa desert and in the eastern part of Mongolia. However, the dust plume released from the Alxa desert did not move far towards the south or the east, as will be discussed in Section 4.2.

For the SD2 event, the accumulated a priori emissions are rather high, especially around the border between China and

15 Mongolia. The maximum emission accumulation here is as high as 370 g/m^2, which results in the overestimation of surface dust concentration and AOD simulation as shown in Fig.3(a.2)-(b.2). In contrast, the posterior simulation estimates that the border region is almost free of dust emission during the event, and the dust plume is actually attributed to the dust emission from the northern Mongolia. Also the Alxa desert contributes partially to the dust plume that effected the FWP region.

For the SD3 event, the a priori emission simulation suggests that most of the dust originates from the source regions in China

20 rather than from the bare regions in Mongolia. Especially in Tengger desert and Alxa desert, the accumulated emissions reach values up to 270 g/m^2. By assimilating the MODIS AOD and PM_{10} data, the posterior dust emission field is updated and the assimilated estimate of the accumulation map is plotted in Fig.6(c.2). What is interesting about the result in the posterior map is that a much smaller amount of dust is estimated to be emitted from Tengger desert and Alxa desert, while sparsely vegetated regions in the northeastern part of the Inner Mongolia province is estimated to be a significant source. Dust from those regions

25 is estimated to be transported towards NCP and Northeast China, as will be discussed later. Close inspection of the posterior emission map show that the emission over the Mongolia and China border region is one of the main source in the SD3 event.

Apart from the spatial patterns of dust emission, the total mass of the emissions from Mongolia and China are calculated and shown in Fig. 6(d), which helps to evaluate the emission intensity of dust in these two countries. Although the spatial patterns have strongly changed by the assimilation of the MODIS and PM_{10} measurements, the posterior emission sums per

30 country and event are in most cases close to the *a priori* values. An except is the value for the China in SD3, for which the total emission is decreased from 15.4 Mton to 5.9 Mton by the assimilation. The emisison sums show that Mongolian deserts are a stronger source of dust (27.2M ton) than the Chinese deserts (18.3M ton).
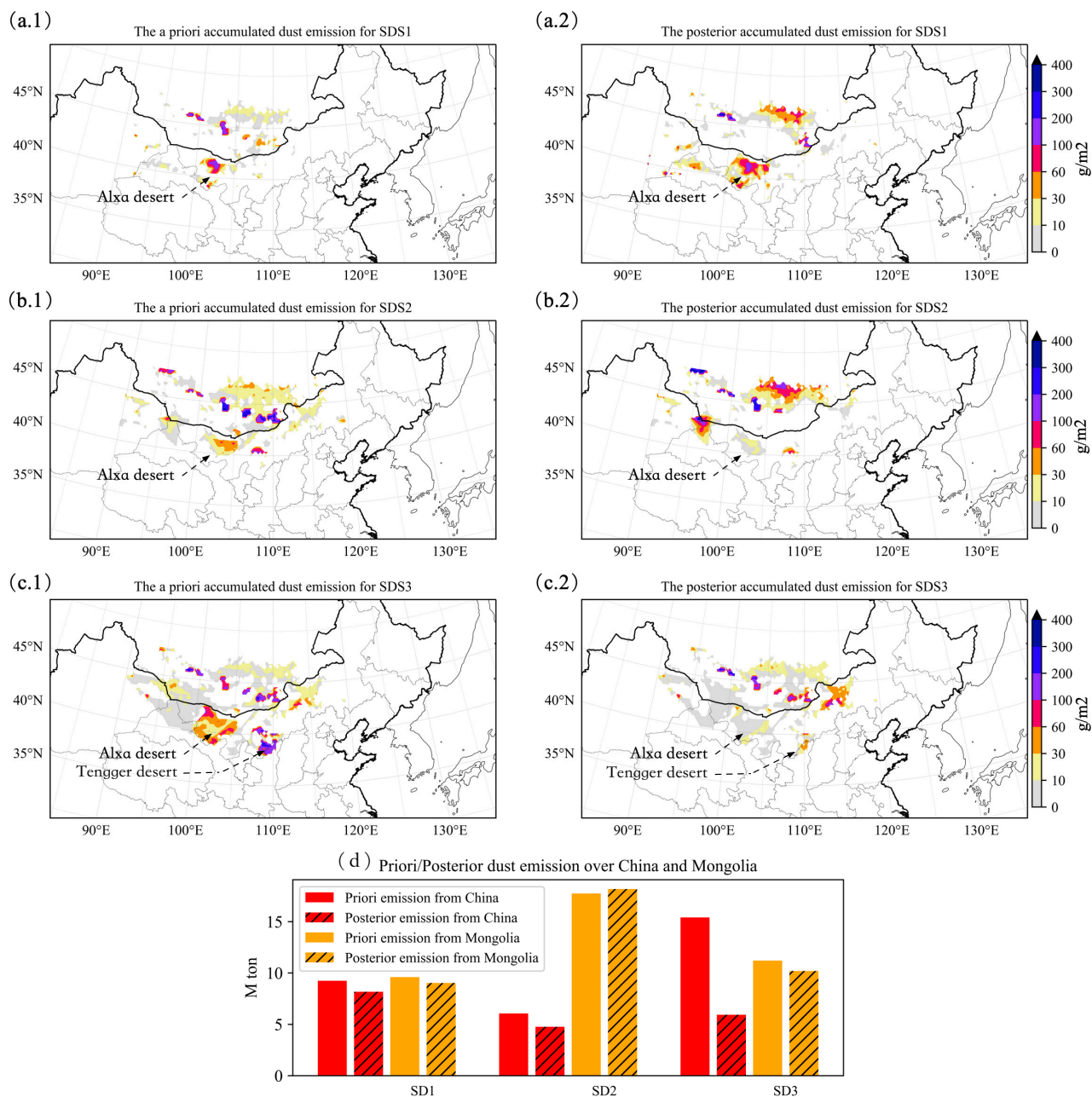
Figure 6. Distribution of the a priori (a.1-c.1) and posterior (a.2-c.2) accumulated dust emission for the SD1, SD2 and SD3; the total priori and posterior emission either from China or from Mongolia during SD1 to SD3 (d).

4.1.2 Simulated dust field

The impact of the assimilation has been evaluated by comparing the simulated observations from the *a priori* and *posterior* simulations with the (bias corrected) observations. The purpose of this paper is to have a emission field as accurate as possible, therefore, we assimilated all available PM_{10} and MODIS AOD observations instead of leaving a subset of them for independent validation. To quantify the performance, the root mean square error (RMSE) that calculates the deviation of the simulation with respect to the bias-corrected measurements is calculated.

A snapshot of the a priori and posterior surface dust concentration and AOD during SD1 are shown in the middle and right panel in Fig.2. Both of the a priori and posterior simulations show a similar pattern as the (bias-corrected) AOD and PM_{10} observations that are shown in Supplementary Fig. S1 and/or the raw data shown in the left panel of Fig. 2. However, the dust concentrations are underestimated in the a priori simulation in the entire region, resulting in a RMSE of 833 $\mu g/m^3$, 1.36 and 1.53. Compared to the a priori simulation, the posterior emission field simulated a more severe dust plume, and the observation-minus-simulation mismatch is reduced to 723 $\mu g/m^3$, 1.30 and 1.33. One important reason for this high error residue is the position mismatch among the simulation and observations. For instance, the plume front (red dash line) that is visilbe in the MODIS AOD retrievals in Fig.2(b.1) is about 100 km ahead of the front line shown in PM_{10} measurements in Fig. 2(a.1). This suggests that the dust plume in the higher layers moves faster, and is in further southeast than the dust cloud at bottom layer. However, this feature is not correctly captured by our LOTOS-EUROS/dust model. Both the simulated plume of AOD and surface dust concentration are in the same position; the simulated plume fronts indicated in Fig.2(a.2) and (b.2) move faster than the front line indicated by PM_{10} measurements, but slower than the front in the MODIS AOD. The two dimensional grid distortion technique developed in Jin et al. (2021) could adjust the position of the dust cloud to better fit with the available measurements, but is not yet able to adjust the vertical structure as is required here. A three dimensional grid distortion should be developed to solve this issue in future.

Fig.3 shows snapshots of original AOD and PM_{10} measurements, as well as the a priori and posterior AOD and surface dust concentration simulation at March 28, 11:00 (CST) within SD2. What stands out in the *a priori* AOD simulation in Fig. 3(a.2) is the overestimation, especially, in the center of the plume in the NCP region. The standard model simulated AOD values even larger than 4, while the measurements are around 2 to 3. It should be noted that all the AOD measurements shown in Fig. 3(a.1) contain both the dust and non-dust fraction, and the baseline-removed AODs which can be found in Fig. S2 are therefore a bit lower. By assimilating these bias-corrected measurements, posterior AOD simulation in Fig.3(a.3) are now in better agreement with the AOD observations. RMSE is therefore reduced from 0.99 in the *a priori* simulation to 0.78 in the *posterior* simulation. The improvement is also seen in the surface PM_{10} simulation, where the RMSE score decreases from 471 $\mu g/m^3$ in the *a priori* to 359 $\mu g/m^3$ in the *posterior* simulation.

Scenes of raw AOD and PM_{10} measurements, the a priori and posterior simulated AOD and surface dust concentration at April 15, 11:00 (CST) during SD3 are plotted in Fig.4. It is apparent from this figure that dust concentrations are overestimated by model during this event as well. For a case in point, the PM_{10} measurements in Fig. 4(b.1) show that FWP is almost free of dust at that moment, and this is confirmed by the baseline-removed PM_{10} measurements shown in Supplementary Fig. S3. The

4DVar assimilation successfully resolves the PM$_{10}$ and AOD measurements. The simulation driven by the posterior emission field is in much better agreement with the measurements, with the PM$_{10}$ RMSE is reduced from 891 μg/m^3 to 144 μg/m^3, and the AOD RMSE drastically decreased from 1.79 to 0.73.

4.2 Source apportionment

5 The dust emission inversion successfully optimized the dust simulation using different types of observations of the dust plumes by adjusting the emission fields. The posterior emission field not only helps us exploit the spatial pattern of active dust sources, but also to simulate the long-distance dust transport more accurate. This could be used for evaluation of the threats that dust imposes on the human health, the transport system, and the Earth system. In this study, we further carry out source apportionment tests based on the estimated emission field. For the two mega-city clusters North China Plain (NCP) and Fenwei

10 Plain (FWP) it has been calculated whether the dust originates from transnational transport from Mongolia or from local sources in China. The locations of NCP and FWP clusters are shown in Fig.1(a); the regions have a population of around 339 and 50 million people, respectively.

Two LOTOS-EUROS/dust simulations have been conducted with the posterior emission field obtained in Section 4.1.1, but with either only the emissions in Mongolia or the emissions in China enabled. Different from cases caused by other pollutants,

15 the spring dust events in East Asia are usually short-term events, with concentrations of dust that quickly increase to huge levels, but also drop down quickly after the storm passed by. Metrics as daily average dust concentration do not reflect the dust intensity directly. Therefore, a dust deposition index is introduced that measures the sum of dry and wet deposition to quantify the impact of the dust in the studied regions.

Fig.7 shows the spatial pattern of the deposition for dust originating from China (left panels) and originating from Mongolia

20 (right panels) in SD1 to SD3. The most interesting finding is that the sources in Mongolia play a much more important role in dust pollution in northern China than the sources in China itself. As shown in panel (a.1), a huge amount of particles has been released in the Alxa desert during SD1, but these were transported westward and almost not effect the densely populated areas. During SD2, the deposition of dust released from China is non-eligible, but the total deposition is still dominant by dust released from Mongolia. During SD3, the dust particles emitted from Chinese deserts were spread all over the northern China

25 and hence played a more significant role.

The total deposition in the NCP and FWP regions has been calculated and is shown in Fig. 7(d). For the NCP region, 49k, 97k, and 50k tons of Mongolia dust were deposited during SD1, SD2, and SD3 events, while the total deposition from Chinese desert is only about 160, 15k, and 74k tons, respectively. For the other important cluster FWP, 2.6k, 20k, and 19k tons attributed to local sources, while 4.3k, 49k, and 4.4k tons of dust are attributed to transnational transport from Mongolia.

30 In general, although the source locations in Mongolia are located further far away from the NCP and FWP regions than the local Chinese deserts, about 58% of the dust deposition is attributed to the transnational transport. Over NCP, this value further grows up to 69%.
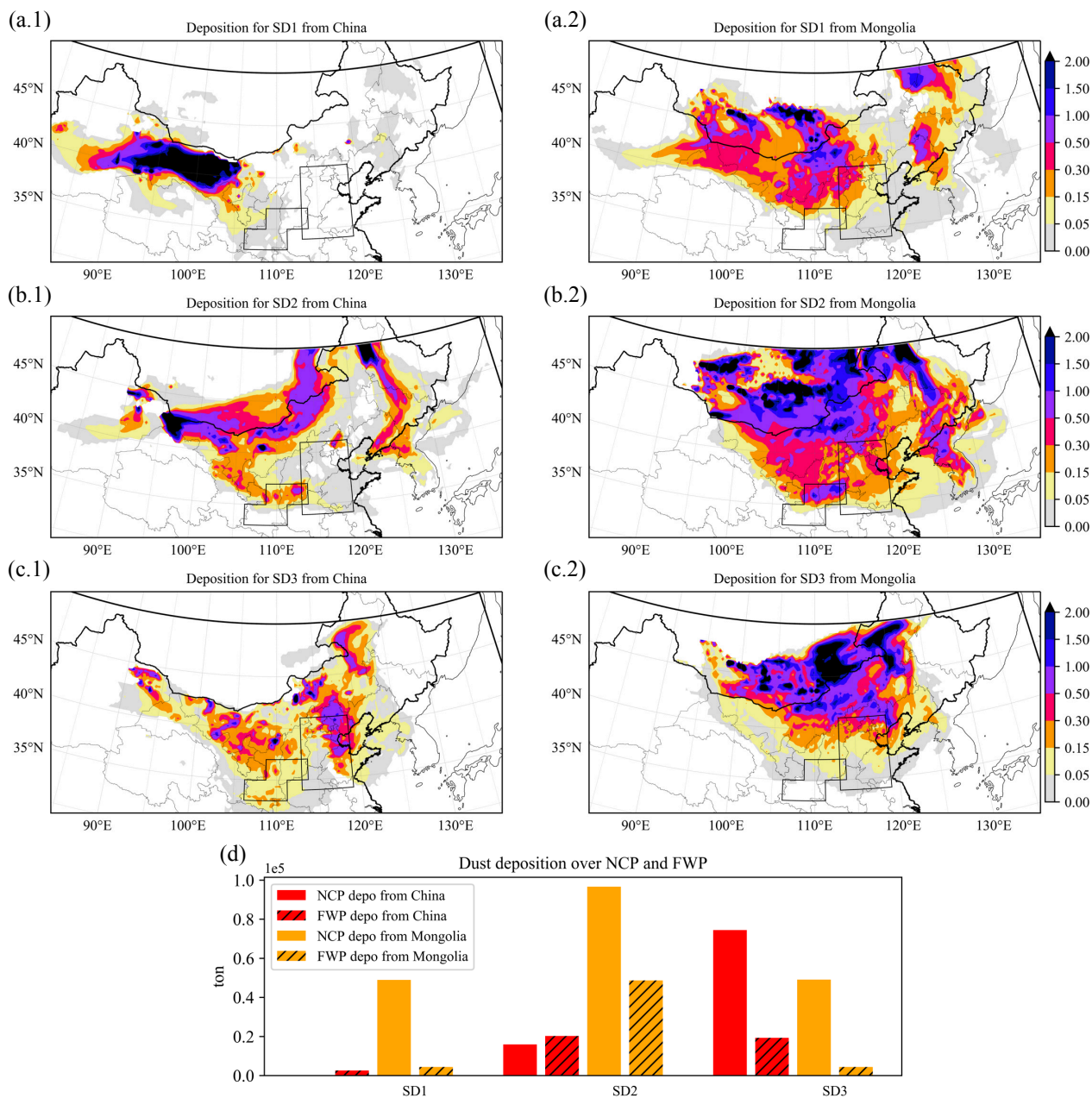
Figure 7. Spatial patterns of deposition of dust originating from China (a.1-c.1) and from Mongolia (a.2-c.2). Panel (d) shows the total mass of dust deposition on NCP and FWP either from China or from Mongolia during SD1 to SD3 (d).

5 Summary and conclusion

In spring 2021, three super dust storms occurred in East Asia after being absent for a (two) decade(s), which brought enormous health damages and property losses, and resulted in profoundly effects to Earth system. To exploit the reappeared super sandstorms, inverse modeling has been conducted through optimizing the dust simulation with observations of satellite AOD and PM_{10} from a surface network. Based on the most likely emission field calculated by the inversion, source apportionment was further performed to derive the contribution of transnational transport from Mongolia and local dust emission to the dust pollutant level in northern China.

Ground-based PM_{10} concentration observations from the Chinese MEP air quality monitoring network, and AOD from the MODIS satellite instrument which has a wide spatial coverage have been assimilated to correct for the uncertainties in the dust emission parametrization. To use MODIS AOD accurately for representing dust optical depth, an AOD data quality control, which includes an Ångström-based data screen and a non-dust AOD bias correction, has been designed and applied before the they are assimilated. The former is capable of selecting the coarse-mode AOD in dusty environment, while the latter aims at removing the non-dust baseline in the selected AOD. The non-dust bias correction is also applied to pre-process the PM_{10} measurements.

An emission inversion has been successfully performed by assimilating those pre-processed measurements. The simulated AOD and surface dust concentration driven by the posterior emission fields have been validated to be in better agreement with the observations. For a further accurate dust field analysis, vertical structure adjusting techniques such as 3D grid distortion are then in demand for fully resolving the ground based PM_{10} and AOD together, and will be explored in our future work. According to the posterior emission field, windblown dust emission occurred actively both in China and Mongolia during the events studied; about 27M ton of dust was released in Mongolian desert, and about 18M ton from the Chinese deserts.

A source apportionment study has been performed based on the posterior emission inventory by estimating the origin of the dust that is deposited in regions in northern China. For the Fenwei Plain (FWP), about 58% of the dust deposition originates from transnational transport from the Mongolian deserts. In the North China Plain (NCP), the local Chinese desert plays an even small role in dust deposition; the long-distance transport from Mongolia contributes is here even 69% while NCP is located further far away from the Mongolia desert.

Code and data availability

The source code and user guide of the LOTOS-EUROS CTM could be obtained from https://lotos-euros.tno.nl. The real-time PM_{10} data are from the network established by the China Ministry of Environmental Protection and available to the public via http://106.37.208.233:20035/. The MODIS Deep Blue C6 data suites are available at https://ladsweb.modaps.eosdis.nasa.gov/. The datasets including measurements and model simulations can be accessed by contacting the corresponding author.

Acknowledgments

This work is supported by the National Natural Science Foundation of China [grant 42105109] and Natural Science Foundation of Jiangsu Province (NO.BK20210664).

Author contribution

5   JJ conceived the study and designed the dust storm data assimilation. JJ, MP and AS performed the control and assimilation tests and carried out the data analysis. AS, HL, WH, BL, and HXL provided useful comments on the paper. JJ prepared the manuscript with contributions from AS and all others co-authors.

Competing interests

The authors declare that they have no conflict of interest.

References

Bessho, K., Date, K., Hayashi, M., Ikeda, A., Imai, T., Inoue, H., Kumagai, Y., Miyakawa, T., Murata, H., Ohno, T., Okuyama, A., Oyama, R., Sasaki, Y., Shimazu, Y., Shimoji, K., Sumida, Y., Suzuki, M., Taniguchi, H., Tsuchiyama, H., Uesawa, D., Yokota, H., and Yoshida, R.: An Introduction to Himawari-8/9— Japan's New-Generation Geostationary Meteorological Satellites, Journal of the Meteorological Society of Japan. Ser. II, 94, 151–183, https://doi.org/10.2151/jmsj.2016-009, http://dx.doi.org/10.2151/jmsj.2016-009, 2016.

Brasseur, G. P., Xie, Y., Petersen, A. K., Bouarar, I., Flemming, J., Gauss, M., Jiang, F., Kouznetsov, R., Kranenburg, R., Mijling, B., Peuch, V.-H., Pommier, M., Segers, A., Sofiev, M., Timmermans, R., van der A, R., Walters, S., Xu, J., and Zhou, G.: Ensemble forecasts of air quality in eastern China – Part 1: Model description and implementation of the MarcoPolo–Panda prediction system, version 1, Geoscientific Model Development, 12, 33–67, https://doi.org/10.5194/gmd-12-33-2019, https://www.geosci-model-dev.net/12/33/2019/, 2019.

Chen, L. and Walsh, M.: Vast sandstorms expose Mongolia's long-ignored ecological crisis, https://asia.nikkei.com/Spotlight/Caixin/Vast-sandstorms-expose-Mongolia-s-long-ignored-ecological-crisis, 2021.

Di Tomaso, E., Nick, Jorba, O., and Garcia-Pando, C. P.: Assimilation of MODIS Dark Target and Deep Blue observations in the dust aerosol component of NMMB-MONARCH version 1.0, Geoscientific Model Development, 10, 1107–1129, https://doi.org/10.5194/gmd-10-1107-2017, https://www.geosci-model-dev.net/10/1107/2017/, 2017.

Di Tomaso, E., Escribano, J., Basart, S., Ginoux, P., Macchia, F., Barnaba, F., Benincasa, F., Bretonnière, P.-A., Buñuel, A., Castrillo, M., Cuevas, E., Formenti, P., Gonçalves, M., Jorba, O., Klose, M., Mona, L., Montané, G., Mytilinaios, M., Obiso, V., Olid, M., Schutgens, N., Votsis, A., Werner, E., and Pérez García-Pando, C.: The MONARCH high-resolution reanalysis of desert dust aerosol over Northern Africa, the Middle East and Europe (2007–2016), Earth System Science Data Discussions, 2021, 1–47, https://doi.org/10.5194/essd-2021-358, https://essd.copernicus.org/preprints/essd-2021-358/, 2021.

Dubovik, O., Smirnov, A., Holben, B., King, M., Kaufman, Y., Eck, T., and Slutsker, I.: Accuracy assessments of aerosol optical properties retrieved from Aerosol Robotic Network (AERONET) Sun and sky radiance measurements, Journal of Geophysical Research: Atmospheres, 105, 9791–9806, 2000.

Dubovik, O., Holben, B., Eck, T. F., Smirnov, A., Kaufman, Y. J., King, M. D., Tanré, D., and Slutsker, I.: Variability of absorption and optical properties of key aerosol types observed in worldwide locations, Journal of the atmospheric sciences, 59, 590–608, 2002.

Eck, T. F., Holben, B., Reid, J., Dubovik, O., Smirnov, A., O'neill, N., Slutsker, I., and Kinne, S.: Wavelength dependence of the optical depth of biomass burning, urban, and desert dust aerosols, Journal of Geophysical Research: Atmospheres, 104, 31 333–31 349, 1999.

Fairlie, T. D., Jacob, D. J., and Park, R. J.: The impact of transpacific transport of mineral dust in the United States, Atmospheric Environment, 41, 1251 – 1266, https://doi.org/https://doi.org/10.1016/j.atmosenv.2006.09.048, 2007.

Ginoux, P., Chin, M., Tegen, I., Prospero, J. M., Holben, B., Dubovik, O., and Lin, S.-J.: Sources and distributions of dust aerosols simulated with the GOCART model, J. Geophys. Res., 106, 20 255–20 273, https://doi.org/10.1029/2000jd000053, http://dx.doi.org/10.1029/2000jd000053, 2001.

Ginoux, P., Prospero, J. M., Gill, T. E., Hsu, N. C., and Zhao, M.: Global-scale attribution of anthropogenic and natural dust sources and their emission rates based on MODIS Deep Blue aerosol products, Reviews of Geophysics, 50, https://doi.org/10.1029/2012RG000388, https://agupubs.onlinelibrary.wiley.com/doi/abs/10.1029/2012RG000388, 2012.

Gkikas, A., Proestakis, E., Amiridis, V., Kazadzis, S., Di Tomaso, E., Tsekeri, A., Marinou, E., Hatzianastassiou, N., and Pérez García-Pando, C.: ModIs Dust AeroSol (MIDAS): a global fine-resolution dust optical depth data set, Atmospheric Measurement Techniques, 14, 309–334, https://doi.org/10.5194/amt-14-309-2021, https://amt.copernicus.org/articles/14/309/2021/, 2021.

Gong, S. L. and Zhang, X. Y.: CUACE/Dust – an integrated system of observation and modeling systems for operational dust forecasting in Asia, Atmospheric Chemistry and Physics, 8, 2333–2340, https://doi.org/10.5194/acp-8-2333-2008, http://dx.doi.org/10.5194/acp-8-2333-2008, 2008.

Han, J., Dai, H., and Gu, Z.: Sandstorms and desertification in Mongolia, an example of future climate events: A review, Environmental Chemistry Letters, pp. 1–11, 2021.

Hsu, N. C., Jeong, M.-J., Bettenhausen, C., Sayer, A. M., Hansell, R., Seftor, C. S., Huang, J., and Tsay, S.-C.: Enhanced Deep Blue aerosol retrieval algorithm: The second generation, Journal of Geophysical Research: Atmospheres, 118, 9296–9315, https://doi.org/10.1002/jgrd.50712, https://agupubs.onlinelibrary.wiley.com/doi/abs/10.1002/jgrd.50712, 2013.

Huneeus, N., Schulz, M., Balkanski, Y., Griesfeller, J., Prospero, J., Kinne, S., Bauer, S., Boucher, O., Chin, M., Dentener, F., Diehl, T., Easter, R., Fillmore, D., Ghan, S., Ginoux, P., Grini, A., Horowitz, L., Koch, D., Krol, M. C., Landing, W., Liu, X., Mahowald, N., Miller, R., Morcrette, J. J., Myhre, G., Penner, J., Perlwitz, J., Stier, P., Takemura, T., and Zender, C. S.: Global dust model intercomparison in AeroCom phase I, Atmospheric Chemistry and Physics, 11, 7781–7816, https://doi.org/10.5194/acp-11-7781-2011, http://dx.doi.org/10.5194/acp-11-7781-2011, 2011.

Jin, G.: The most severe Sandstorm in a decade, https://www.chinanews.com/m/sh/2021/03-15/9433005.shtml, 2021.

Jin, J., Lin, H. X., Heemink, A., and Segers, A.: Spatially varying parameter estimation for dust emissions using reduced-tangent-linearization 4DVar, Atmospheric Environment, 187, 358–373, https://doi.org/https://doi.org/10.1016/j.atmosenv.2018.05.060, https://www.sciencedirect.com/science/article/pii/S1352231018303704, 2018.

Jin, J., Lin, H. X., Segers, A., Xie, Y., and Heemink, A.: Machine learning for observation bias correction with application to dust storm data assimilation, Atmospheric Chemistry and Physics, 19, 10 009–10 026, https://doi.org/10.5194/acp-19-10009-2019, https://www.atmos-chem-phys.net/19/10009/2019/, 2019a.

Jin, J., Segers, A., Heemink, A., Yoshida, M., Han, W., and Lin, H.-X.: Dust Emission Inversion Using Himawari-8 AODs Over East Asia: An Extreme Dust Event in May 2017, Journal of Advances in Modeling Earth Systems, 11, 446–467, https://doi.org/10.1029/2018MS001491, https://agupubs.onlinelibrary.wiley.com/doi/full/10.1029/2018MS001491, 2019b.

Jin, J., Segers, A., Liao, H., Heemink, A., Kranenburg, R., and Lin, H. X.: Source backtracking for dust storm emission inversion using an adjoint method: case study of Northeast China, Atmospheric Chemistry and Physics, 20, 15 207–15 225, https://doi.org/10.5194/acp-20-15207-2020, https://acp.copernicus.org/articles/20/15207/2020/, 2020.

Jin, J., Segers, A., Lin, H. X., Henzing, B., Wang, X., Heemink, A., and Liao, H.: Position correction in dust storm forecast using LOTOS-EUROS v2.1: grid distorted data assimilation v1.0, Geoscientific Model Development Discussions, 2021, 1–25, https://doi.org/10.5194/gmd-2021-10, https://gmd.copernicus.org/preprints/gmd-2021-10/, 2021.

Justice, C., Vermote, E., Townshend, J., Defries, R., Roy, D., Hall, D., Salomonson, V., Privette, J., Riggs, G., Strahler, A., Lucht, W., Myneni, R., Knyazikhin, Y., Running, S., Nemani, R., Wan, Z., Huete, A., van Leeuwen, W., Wolfe, R., Giglio, L., Muller, J., Lewis, P., and Barnsley, M.: The Moderate Resolution Imaging Spectroradiometer (MODIS): land remote sensing for global change research, IEEE Transactions on Geoscience and Remote Sensing, 36, 1228–1249, https://doi.org/10.1109/36.701075, 1998.

Kalnay, E.: Atmospheric Modeling, Data Assimilation and Predictability, Cambridge University Press, https://doi.org/10.1017/CBO9780511802270, 2002.

Li, Z., Xu, H., Li, K., Li, D., Xie, Y., Li, L., Zhang, Y., Gu, X., Zhao, W., Tian, Q., et al.: Comprehensive study of optical, physical, chemical, and radiative properties of total columnar atmospheric aerosols over China: An overview of Sun–Sky Radiometer Observation Network (SONET) measurements, Bulletin of the American Meteorological Society, 99, 739–755, 2018.

Lin, C., Wang, Z., and Zhu, J.: An Ensemble Kalman Filter for severe dust storm data assimilation over China, Atmospheric Chemistry & Physics, 8, 2975–2983, https://www.atmos-chem-phys.net/8/2975/2008/, 2008.

Liu, M., Zhou, G., Saari, R. K., Li, S., Liu, X., and Li, J.: Quantifying PM2.5 mass concentration and particle radius using satellite data and an optical-mass conversion algorithm, ISPRS Journal of Photogrammetry and Remote Sensing, 158, 90 – 98, https://doi.org/https://doi.org/10.1016/j.isprsjprs.2019.10.010, http://www.sciencedirect.com/science/article/pii/S0924271619302461, 2019.

Lorente-Plazas, R. and Hacker, J. P.: Observation and Model Bias Estimation in the Presence of Either or Both Sources of Error, Monthly Weather Review, 145, 2683–2696, https://doi.org/10.1175/MWR-D-16-0273.1, http://dx.doi.org/10.1175/MWR-D-16-0273.1, 2017.

Manders, A. M. M., Builtjes, P. J. H., Curier, L., Denier van der Gon, H. A. C., Hendriks, C., Jonkers, S., Kranenburg, R., Kuenen, J., Segers, A. J., Timmermans, R. M. A., Visschedijk, A., Wichink Kruit, R. J., Van Pul, W. A. J., Sauter, F. J., van der Swaluw, E., Swart, D. P. J., Douros, J., Eskes, H., van Meijgaard, E., van Ulft, B., van Velthoven, P., Banzhaf, S., Mues, A., Stern, R., Fu, G., Lu, S., Heemink, A., van Velzen, N., and Schaap, M.: Curriculum vitae of the LOTOS-EUROS (v2.0) chemistry transport model, Geoscientific Model Development, 10, 4145–4173, https://doi.org/10.5194/gmd-10-4145-2017, http://www.geosci-model-dev-discuss.net/gmd-2017-88/, 2017.

Marticorena, B. and Bergametti, G.: Modeling the atmospheric dust cycle: 1. Design of a soil-derived dust emission scheme, J. Geophys. Res., 100, 16 415–16 430, https://doi.org/10.1029/95JD00690, http://dx.doi.org/10.1029/95JD00690, 1995.

Min, M., Wu, C., Li, C., Liu, H., Xu, N., Wu, X., Chen, L., Wang, F., Sun, F., Qin, D., et al.: Developing the science product algorithm testbed for Chinese next-generation geostationary meteorological satellites: Fengyun-4 series, Journal of Meteorological Research, 31, 708–719, 2017.

Mona, L., Papagiannopoulos, N., Basart, S., Baldasano, J., Binietoglou, I., Cornacchia, C., and Pappalardo, G.: EARLINET dust observations vs. BSC-DREAM8b modeled profiles: 12-year-long systematic comparison at Potenza, Italy, Atmospheric Chemistry and Physics, 14, 8781–8793, https://doi.org/10.5194/acp-14-8781-2014, https://www.atmos-chem-phys.net/14/8781/2014/, 2014.

Morcrette, J.-J., Beljaars, A., Benedetti, A., Jones, L., and Boucher, O.: Sea-salt and dust aerosols in the ECMWF IFS model, Geophysical Research Letters, 35, https://doi.org/10.1029/2008GL036041, https://agupubs.onlinelibrary.wiley.com/doi/abs/10.1029/2008GL036041, 2008a.

Morcrette, J.-J., Boucher, O., Jones, L., Salmond, D., Bechtold, P., Beljaars, A., Benedetti, A., Bonet, A., Kaiser, J., Razinger, M., Schulz, M., Serrar, S., Simmons, A., Sofiev, M., Suttie, M., Tompkins, A., Untch, A., and the GEMS-AER team: Aerosol analysis and forecast in the ECMWF Integrated Forecast System: Forward modelling., ECMWF Technical Memoranda, p. 35, https://doi.org/10.21957/jxqm3uq6j, https://www.ecmwf.int/node/11281, 2008b.

Morcrette, J.-J., Boucher, O., Jones, L., Salmond, D., Bechtold, P., Beljaars, A., Benedetti, A., Bonet, A., Kaiser, J. W., Razinger, M., Schulz, M., Serrar, S., Simmons, A. J., Sofiev, M., Suttie, M., Tompkins, A. M., and Untch, A.: Aerosol analysis and forecast in the European Centre for Medium-Range Weather Forecasts Integrated Forecast System: Forward modeling, Journal of Geophysical Research: Atmospheres, 114, https://doi.org/10.1029/2008JD011235, https://agupubs.onlinelibrary.wiley.com/doi/abs/10.1029/2008JD011235, 2009.

Niu, T., Gong, S. L., Zhu, G. F., Liu, H. L., Hu, X. Q., Zhou, C. H., and Wang, Y. Q.: Data assimilation of dust aerosol observations for the CUACE/dust forecasting system, Atmospheric Chemistry and Physics, 8, 3473–3482, https://doi.org/10.5194/acp-8-3473-2008, http://dx.doi.org/10.5194/acp-8-3473-2008, 2008.

Pérez, C., Nickovic, S., Baldasano, J. M., Sicard, M., Rocadenbosch, F., and Cachorro, V. E.: A long Saharan dust event over the western Mediterranean: Lidar, Sun photometer observations, and regional dust modeling, Journal of Geophysical Research: Atmospheres, 111, https://doi.org/10.1029/2005JD006579, https://agupubs.onlinelibrary.wiley.com/doi/abs/10.1029/2005JD006579, 2006.

Remer, L. A., Kaufman, Y. J., Tanré, D., Mattoo, S., Chu, D. A., Martins, J. V., Li, R. R., Ichoku, C., Levy, R. C., Kleidman, R. G., Eck, T. F., Vermote, E., and Holben, B. N.: The MODIS Aerosol Algorithm, Products, and Validation, Journal of the Atmospheric Sciences, 62, 947–973, 2005.

Saide, P. E., Carmichael, G. R., Liu, Z., Schwartz, C. S., Lin, H. C., da Silva, A. M., and Hyer, E.: Aerosol optical depth assimilation for a size-resolved sectional model: impacts of observationally constrained, multi-wavelength and fine mode retrievals on regional scale analyses and forecasts, Atmospheric Chemistry and Physics, 13, 10 425–10 444, https://doi.org/10.5194/acp-13-10425-2013, https://www.atmos-chem-phys.net/13/10425/2013/, 2013.

Sayer, A. M., Munchak, L. A., Hsu, N. C., Levy, R. C., Bettenhausen, C., and Jeong, M.-J.: MODIS Collection 6 aerosol products: Comparison between Aqua's e-Deep Blue, Dark Target, and "merged" data sets, and usage recommendations, Journal of Geophysical Research: Atmospheres, 119, 13,965–13,989, https://doi.org/10.1002/2014JD022453, https://agupubs.onlinelibrary.wiley.com/doi/abs/10.1002/2014JD022453, 2014.

Schepanski, K., Tegen, I., Laurent, B., Heinold, B., and Macke, A.: A new Saharan dust source activation frequency map derived from MSG-SEVIRI IR-channels, Geophysical Research Letters, 34, 2007.

Schuster, G. L., Dubovik, O., and Holben, B. N.: Angstrom exponent and bimodal aerosol size distributions, Journal of Geophysical Research: Atmospheres, 111, https://doi.org/10.1029/2005JD006328, https://agupubs.onlinelibrary.wiley.com/doi/abs/10.1029/2005JD006328, 2006.

Shao, Y.: Simplification of a dust emission scheme and comparison with data, J. Geophys. Res., 109, D10 202+, https://doi.org/10.1029/2003jd004372, http://dx.doi.org/10.1029/2003jd004372, 2004.

Shao, Y., Raupach, M. R., and Findlater, P. A.: Effect of saltation bombardment on the entrainment of dust by wind, J. Geophys. Res., 98, 12+, https://doi.org/10.1029/93jd00396, http://dx.doi.org/10.1029/93jd00396, 1993.

Shao, Y., Wyrwoll, K.-H., Chappell, A., Huang, J., Lin, Z., McTainsh, G. H., Mikami, M., Tanaka, T. Y., Wang, X., and Yoon, S.: Dust cycle: An emerging core theme in Earth system science, Aeolian Research, 2, 181 – 204, https://doi.org/https://doi.org/10.1016/j.aeolia.2011.02.001, http://www.sciencedirect.com/science/article/pii/S1875963711000085, 2011.

Shao, Y., Klose, M., and Wyrwoll, K.-H.: Recent global dust trend and connections to climate forcing, Journal of Geophysical Research: Atmospheres, 118, 11,107–11,118, https://doi.org/https://doi.org/10.1002/jgrd.50836, https://agupubs.onlinelibrary.wiley.com/doi/abs/10.1002/jgrd.50836, 2013.

Shao, Y. P., Raupach, M. R., and Leys, J. F.: A model for predicting aeolian sand drift and dust entrainment on scales from paddock to region, Australian Journal of Soil Research, 34, 309+, https://doi.org/10.1071/sr9960309, http://dx.doi.org/10.1071/sr9960309, 1996.

Timmermans, R., Kranenburg, R., Manders, A., Hendriks, C., Segers, A., Dammers, E., Zhang, Q., Wang, L., Liu, Z., Zeng, L., Denier van der Gon, H., and Schaap, M.: Source apportionment of PM2.5 across China using LOTOS-EUROS, Atmospheric Environment, https://doi.org/10.1016/j.atmosenv.2017.06.003, http://dx.doi.org/10.1016/j.atmosenv.2017.06.003, 2017.

Winker, D. M., Hunt, W. H., and McGill, M. J.: Initial performance assessment of CALIOP, Geophysical Research Letters, 34, L19 803+, https://doi.org/10.1029/2007gl030135, http://dx.doi.org/10.1029/2007gl030135, 2007.

World Meteorological Organization: WMO AIRBORNE DUST BULLETIN: Sand and Dust Storm Warning Advisory and Assessment System, https://library.wmo.int/doc_num.php?explnum_id=3416, 2017.

World Meteorological Organization: WMO AIRBORNE DUST BULLETIN: Sand and Dust Storm Warning Advisory and Assessment System, Tech. rep., https://public.wmo.int/en/resources/library/wmo-airborne-dust-bulletin-sand-and-dust-storm-warning-advisory-and-assessment, 2019.

World Meteorological Organization: Sand and Dust Storm Warning Advisory and Assessment System: Science Progress Report, Tech. rep., World Meteorological Organization, https://public.wmo.int/en/resources/library/sand-and-dust-storm-warning-advisory-and-assessment-system-science-progress-report, 2020.

Wu, C., Lin, Z., He, J., Zhang, M., Liu, X., Zhang, R., and Brown, H.: A process-oriented evaluation of dust emission parameterizations in CESM: Simulation of a typical severe dust storm in East Asia, Journal of Advances in Modeling Earth Systems, 8, 1432–1452, https://doi.org/10.1002/2016MS000723, https://www.google.nl/_/chrome/newtab?espv=2&ie=UTF-8, 2016.

Yin, Z., Wan, Y., Zhang, Y., and Wang, H.: Why super sandstorm 2021 in North China, National Science Review, https://doi.org/10.1093/nsr/nwab165, https://doi.org/10.1093/nsr/nwab165, nwab165, 2021.

Yumimoto, K. and Takemura, T.: Long-term inverse modeling of Asian dust: Interannual variations of its emission, transport, deposition, and radiative forcing, J. Geophys. Res. Atmos., 120, 2014JD022 390+, https://doi.org/10.1002/2014jd022390, http://dx.doi.org/10.1002/2014jd022390, 2015.

Yumimoto, K., Nagao, T. M., Kikuchi, M., Sekiyama, T. T., Murakami, H., Tanaka, T. Y., Ogi, A., Irie, H., Khatri, P., Okumura, H., Arai, K., Morino, I., Uchino, O., and Maki, T.: Aerosol data assimilation using data from Himawari-8, a next-generation geostationary meteorological satellite, Geophys. Res. Lett., 43, 2016GL069 298+, https://doi.org/10.1002/2016gl069298, http://dx.doi.org/10.1002/2016gl069298, 2016.

Zender, C. S.: Mineral Dust Entrainment and Deposition (DEAD) model: Description and 1990s dust climatology, Journal of Geophysical Research, 108, 4416+, https://doi.org/10.1029/2002jd002775, http://dx.doi.org/10.1029/2002jd002775, 2003.

Zhang, X. X., Sharratt, B., Liu, L. Y., Wang, Z. F., Pan, X. L., Lei, J. Q., Wu, S. X., Huang, S. Y., Guo, Y. H., Li, J., Tang, X., Yang, T., Tian, Y., Chen, X. S., Hao, J. Q., Zheng, H. T., Yang, Y. Y., and Lyu, Y. L.: East Asian dust storm in May 2017: observations, modelling, and its influence on the Asia-Pacific region, Atmospheric Chemistry and Physics, 18, 8353–8371, https://www.atmos-chem-phys.net/18/8353/2018/, 2018.

Zhang, Z., Wu, W., Fan, M., Tao, M., Wei, J., Jin, J., Tan, Y., and Wang, Q.: Validation of Himawari-8 aerosol optical depth retrievals over China, Atmospheric environment, 199, 32–44, 2019.

Zhou, C. H., Gong, S. L., Zhang, X. Y., Wang, Y. Q., Niu, T., Liu, H. L., Zhao, T. L., Yang, Y. Q., and Hou, Q.: Development and evaluation of an operational SDS forecasting system for East Asia: CUACE/Dust, Atmospheric Chemistry and Physics, 8, 787–798, https://doi.org/10.5194/acp-8-787-2008, http://dx.doi.org/10.5194/acp-8-787-2008, 2008.